Journal of Applied Physics ARTICLE scitation.org/journal/jap

Theory of laser-induced photoemission from a metal surface with nanoscale dielectric coating

Cite as: J. Appl. Phys. **131**, 064903 (2022); doi: 10.1063/5.0078060
Submitted: 9 November 2021 · Accepted: 22 January 2022 ·
Published Online: 10 February 2022

Yang Zhou and Peng Zhang[a)]

AFFILIATIONS

Department of Electrical and Computer Engineering, Michigan State University, East Lansing, Michigan 48824-1226, USA

[a)]**Author to whom correspondence should be addressed:** pz@egr.msu.edu

ABSTRACT

This paper presents an analytical quantum model for photoemission from metal surfaces coated with an ultrathin dielectric, by solving the 1D time-dependent Schrödinger equation subject to an oscillating double-triangular potential barrier. The model is valid for an arbitrary combination of metal (of any work function and Fermi level), dielectric (of any thickness, relative permittivity, and electron affinity), laser field (strength and wavelength), and dc field. The effects of dielectric properties on photoemission are systematically investigated. It is found that a flat metal surface with dielectric coating can photoemit a larger current density than the uncoated case when the dielectric has smaller relative permittivity and larger electron affinity. Resonant peaks in the photoemission probability and emission current are observed as a function of dielectric thickness or electron affinity due to the quantum interference of electron waves inside the dielectric. Our model is compared with the effective single-barrier quantum model and modified Fowler–Nordheim equation, for both 1D flat cathodes and pyramid-shaped nanoemitters. While the three models show quantitatively good agreement in the optical field tunneling regime, the present model may be used to give a more accurate evaluation of photoemission from coated emitters in the multiphoton absorption regime.

I. INTRODUCTION

Photoelectron emission is important to applications such as dielectric laser accelerators,[1–3] free electron lasers (FELs),[4,5] ultrashort x-ray sources,[6] time-resolved electron microscopes,[7–10] ultrafast electron diffraction,[11] carrier-envelope detection,[12–16] and novel nano-electronics.[17–23] While enabling the exploration of matter at a temporal resolution of femtosecond and a spatial resolution of nanometer,[24–27] those applications rely on high-performance photocathodes or photoemitters, which are required to be of high efficiency and high stability.[28–30] Coatings, such as graphene, nano-diamond, silicon dioxides, and zinc dioxides, are proposed to be fabricated atop cathodes to protect them from degradation by ion and electron bombardment, or oxidization under poor vacuum conditions.[31–35] Coatings not only elongate the operational lifetime and the current stability of photocathodes but also enhance the quantum efficiency of photoemission by the lowering of the effective work function or the enhancement of the laser field.[31,32,36–38] Analogous heterostructure photocathodes are prospective to optimize the quantum yield and emittance simultaneously for electron sources in x-ray free-electron lasers.[29,39]

The development of theory for photoemission from coated cathodes facilitates the optimization of the design and performance of photocathodes. Commonly used Fowler–Nordheim-type equations, which assume photoelectron emission occurring in positive half cycles of the intense laser, are applicable only in the optical field tunneling regime but not in the multiphoton absorption regime.[40] Furthermore, it has been shown that negative half cycles also play a role in the photoemission process.[16] Therefore, an exact model for photoemission from cathode's with ultrathin coatings is desirable to uncover the interplay of various parameters on photoemission and provide insights into the development of photocathodes.

In this study, we construct an exact analytical quantum model for laser-driven photoemission from cathodes coated with a nanoscale-thick dielectric by solving the time-dependent Schrödinger equation (TDSE). The model is applicable to photoemission for arbitrary combinations of metal properties (i.e., work function and Fermi level), dielectric properties (i.e., thickness, relative permittivity, and electron affinity), laser field (i.e., wavelength, and field strength or intensity), and dc field. Based on the analytical solution, we investigate the effects of dielectric properties on

photoemission. This analytical model is compared with the effective single-triangular barrier model[36] and modified Fowler–Nordheim equation[40,41] for photoemission from a dielectric-coated flat metal surface and a dielectric-coated pyramid-shaped nanoemitter.

II. THEORETICAL FORMULATION

In the one-dimensional (1D) model (see Fig. 1), electrons with initial longitudinal energy ε are emitted from the flat metal surface coated with a nanoscale-thick dielectric, driven by a laser field and a dc bias. The laser field and dc bias field are perpendicular to the metal surface. For simplicity, the scattering effects of photoexcited electrons with other electrons and phonons in the metal and dielectric, the charge trapping effect in the dielectric, are ignored.[16,42,43] Therefore, the time-varying potential barrier in those three regions, i.e., metal, dielectric, and vacuum, reads

$$\phi(x,t)=\begin{cases}0, & x<0,\\ V_0-\chi-eF_0^{diel}x-eF_1^{diel}x\cos\omega t, & 0\le x<d,\\ V_0+ed(F_0-F_0^{diel})+ed(F_1-F_1^{diel})\cos\omega t-eF_0x-eF_1x\cos\omega t, & x\ge d,\end{cases} \tag{1}$$

where $V_0=W+E_F$, with E_F being the Fermi energy of the metal and $W=W_0-\Delta W$ being the effective work function including the potential barrier lowering by the Schottky effect due to the dc electric field F_0, $\Delta W=2\sqrt{e^3F_0^{diel}/16\pi\varepsilon_0\varepsilon_{diel}}$ when the maximum of the potential barrier including image charge potential is in the coating or $\Delta W=2\sqrt{e^3F_0^{diel}/16\pi\varepsilon_0}$ when the maximum is in the vacuum; χ is the electron affinity of the dielectric; e is the positive elementary charge; F_0 and F_1 are the dc electric field and laser electric field in the vacuum, respectively; F_0^{diel} and F_1^{diel} are the dc and laser electric field inside the dielectric, respectively; ω is the angular frequency of the laser field; and d is the thickness of the dielectric. For a perfectly flat surface, $F_0^{diel}=F_0/\varepsilon_{diel}$ and $F_1^{diel}=F_1/\varepsilon_{diel}$ inside the dielectric with ε_{diel} being the relative permittivity of the dielectric.

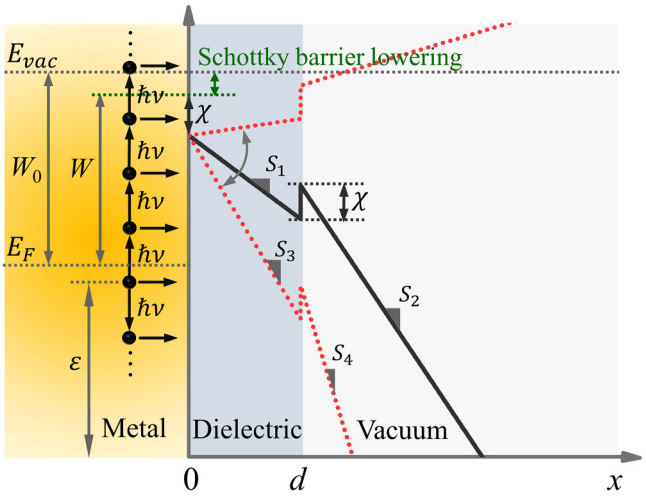

FIG. 1. Photoemission from a flat metal surface coated with a dielectric under a laser electric field and dc bias. The metal–dielectric interface is located at $x=0$, and the coating's thickness is d. The metal has a Fermi energy E_F and a nominal work function of W_0. The effective work function $W=W_0-\Delta W$, with the Schottky barrier lowering $\Delta W=2\sqrt{e^3F_0^{diel}/16\pi\varepsilon_0\varepsilon_{diel}}$ when the maximum of the potential barrier including image charge potential is in the coating or $\Delta W=2\sqrt{e^3F_0/16\pi\varepsilon_0}$ when the potential maximum is in the vacuum. The dielectric has an electron affinity of χ and a relative permittivity of ε_{diel}. The laser field strengths are F_1 in the vacuum and F_1^{diel} in the coating. The dc field strengths are F_0 in the vacuum and F_0^{diel} in the coating. The electron incident longitudinal energy is ε. The black solid line represents the potential profile under the dc field F_0 only, and the red dotted lines are for the time-dependent potential profile due to both F_0 and F_1. Slopes of the potential profile, denoted as S_1, S_2, S_3, and S_4, are $-eF_0^{diel}$, $-eF_0$, $-e(F_0^{diel}+F_1^{diel})$, and $-e(F_0+F_1)$, respectively.

The electron wave functions $\psi(x,t)$ in the metal, dielectric, and vacuum are obtained by solving the time-dependent Schrödinger equation (see Appendix A for solutions),

$$i\hbar\frac{\partial\psi(x,t)}{\partial t}=-\frac{\hbar^2}{2m}\frac{\partial^2\psi(x,t)}{\partial x^2}+\phi(x,t)\psi(x,t), \tag{2}$$

where $\hbar$ is the reduced Planck's constant; m is the electron effective mass, set to the electron rest mass in all three regions for simplicity; and $\phi(x,t)$ is the potential given in Eq. (1).

The electron transmission probability, $w(\varepsilon,x,t)=J_v(\varepsilon,x,t)/J_i(\varepsilon)$, is defined as the ratio of transmitted electron probability current density in the vacuum J_v to the incident electron probability current density in the metal J_i, both of which are calculated from the electron probability current density $J=i\hbar/2m(\psi\nabla\psi^*-\psi^*\nabla\psi)$. It is easy to show the time-averaged transmission probability as

$$D(\varepsilon)=\sum_{n=-\infty}^{\infty}w_n(\varepsilon),\quad w_n(\varepsilon)=\frac{1}{k_0}Im\left[i\sqrt{\frac{2m}{\hbar^2}E_{3n}}|T_{3n}|^2\right]\ \text{for } F_0=0, \tag{3a}$$

or

$$D(\varepsilon)=\sum_{n=-\infty}^{\infty}w_n(\varepsilon),\quad w_n(\varepsilon)=\frac{|T_{3n}|^2}{k_0}Im\left[\frac{i\kappa_3}{\pi}\right]\ \text{for } F_0\neq 0, \tag{3b}$$

with $k_0=\sqrt{\frac{2m\varepsilon}{\hbar^2}}$; $E_{3n}=\varepsilon+n\hbar\omega-U_{p3}-V_{30}$ is the drift kinetic energy in the vacuum, with the ponderomotive energy $U_{p3}=\frac{e^2F_1^2}{4m\omega^2}$

and $V_{30} = W + E_F + ed(F_0 - F_0^{diel})$ for $F_0 \neq 0$ or $V_{30} = W_0 + E_F$ for $F_0 = 0$; and $\kappa_3 = \left(\frac{2meF_0}{\hbar^2}\right)^{1/3}$; T_{3n} is the transmission coefficient of the wave in the vacuum (see Appendix A for more details).

The electron emission current density is obtained from

$$J = e\int_0^\infty D(\varepsilon)N(\varepsilon)d\varepsilon, \tag{4}$$

where $D(\varepsilon)$ is given in Eq. (3) and $N(\varepsilon) = \frac{mk_BT}{2\pi^2\hbar^3}\ln\left[1+\exp\left(\frac{E_F-\varepsilon}{k_BT}\right)\right]$ is the flux of electrons impinging normal to the metal–dielectric interface, which is calculated from the three-dimensional (3D) free electron theory of metal,[43–45] with k_B being the Boltzmann's constant and T being the temperature.

III. RESULTS

Based on the theory developed in Sec. II, we provide an analysis of the photoemission from metallic cathodes coated with dielectric. The metal is assumed to be gold, with nominal work function $W_0 = 5.1$ eV and Fermi energy $E_F = 5.53$ eV. The laser has a wavelength of 800 nm, corresponding to the photon energy of 1.55 eV. These are the default properties of the metal and laser respectively, unless prescribed otherwise.

A. Effects of dielectric properties on photoemission from a flat metal surface

Figure 2 shows the effects of coating dielectric properties (i.e., thickness d, relative permittivity ε_{diel}, and electron affinity χ) on the electron transmission probability from a flat metal surface. Since most of the photoemission occurs with electron initial energies near the Fermi level at ambient temperature, the free electrons inside the metal are assumed to have an initial energy $\varepsilon = E_F$. The electron transmission probability through the nth channel $w_n(\varepsilon = E_F)$ calculated from Eq. (3), for the dielectrics of a different thickness d, relative permittivity ε_{diel}, and electron affinity χ, is plotted in Figs. 2(a)–2(c), respectively. The laser has a field strength of $F_1 = 5$ V/nm. The dc electric field is $F_0 = 0$. It is found that the dominant photoemission is through four-photon absorption ($n = 4$) under the fields provided, regardless of the dielectric properties. By checking the Keldysh parameter γ, it is found that $\gamma \geq 3.59$ for all the cases in Figs. 2(a)–2(c) (see Fig. S8 in the supplementary material), indicating multiphoton absorption process. The dominant channel, $n = 4$, is consistent with the ratio of the work function to the photon energy $\langle W/\hbar\omega \rangle$, where $\langle\rangle$ represents the next nearest integer to the value inside the bracket. $w_n(\varepsilon = E_F)$ increases with decreasing ε_{diel} or increasing χ, due to the narrowed or reduced barrier in the dielectric, which is similar to dc field emission from thin dielectric-coated

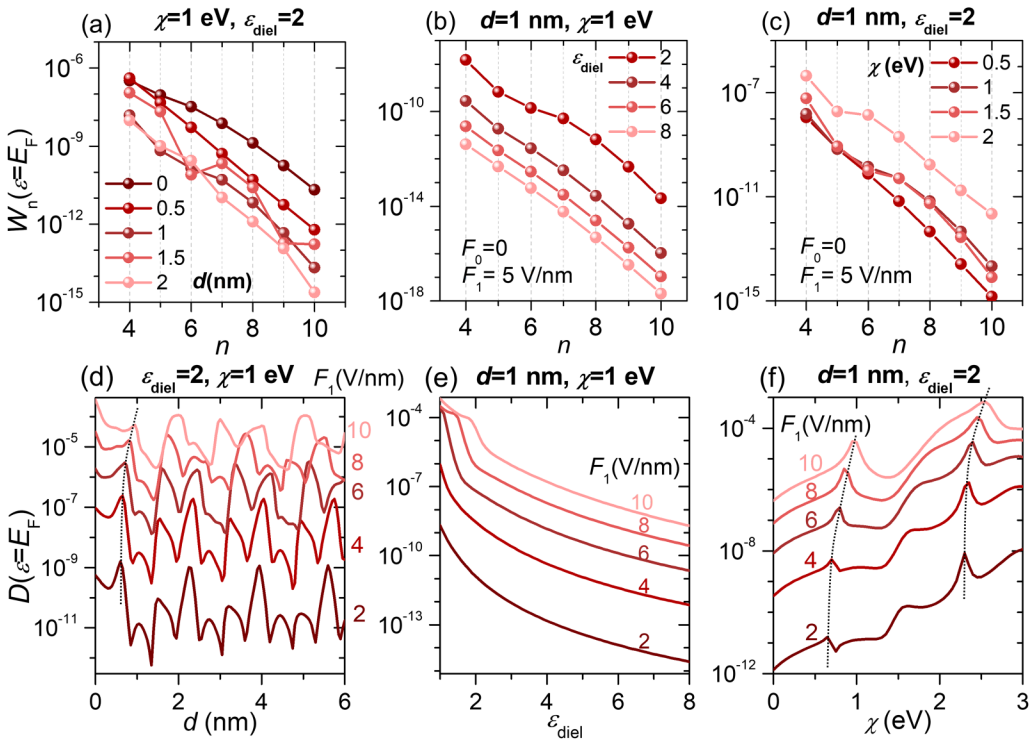

FIG. 2. Effects of dielectric properties on the photoelectron transmission probability from a flat metal surface. Time-averaged electron transmission probability through the nth channel, w_n, calculated from Eq. (3), for a dielectric of a different (a) thickness d; (b) relative permittivity ε_{diel}; and (c) electron affinity χ. The photoelectron transmission probability $D(\varepsilon = E_F)$ calculated from Eq. (3), as a function of dielectric properties (d) thickness d; (e) relative permittivity ε_{diel}; and (f) electron affinity χ, for various laser field strengths. The dc electric field $F_0 = 0$.

surfaces.[38] However, $w_n(\varepsilon = E_F)$ has no clear monotonic dependence on d, as shown in Fig. 2(a).

The electron transmission probability $D(\varepsilon = E_F)$, which is the sum of w_n over all channels, is presented as a function of dielectric thickness, relative permittivity, and electron affinity in Figs. 2(d)–2(f), respectively, under various laser field strengths F_1 [see Fig. S1 in the supplementary material $D(\varepsilon = E_F)$ vs F_1]. It is obvious that the transmission probability increases when the laser field strength increases. In Fig. 2(d), the transmission probability shows approximately periodic peaks with respect to the dielectric thickness. These peaks are due to resonance in the quantum interference[46] between electron waves transmitted to and reflected from the dielectric–vacuum interface, which forms constructive interference when the dielectric is of a particular thickness (see Figs. S2 and S4 in the supplementary material). As the laser field strength increases, peaks on the curves shift toward larger thicknesses, as indicated by the gray dotted line in Fig. 2(d). The physics behind this shift lies in the fact that the wavelength of the electron waves inside the dielectric increases with the laser field (see Fig. S3 in the supplementary material), which can also be indicated by the wavenumber $\sqrt{2mE_{2n}/\hbar^2}$, with $E_{2n} = \varepsilon + n\hbar\omega - U_{p2} - (E_F + W - \chi)$ and $U_{p2} = e^2(F_1^{diel})^2/4m\omega^2$.

Figure 2(e) shows that the transmission probability $D(\varepsilon = E_F)$ decreases with the relative permittivity of the dielectric ε_{diel} for a given laser field, due to the smaller field $F_1^{diel} = F_1/\varepsilon_{diel}$ inside the dielectric. When ε_{diel} is large, e.g., $\varepsilon_{diel} > 2$, F_1^{diel} inside the dielectric would be relatively small for a given F_1; thus, the incident electron would see a double-triangular potential barrier before emission (see Fig. 1), yielding a rapidly decreasing slope in $D(\varepsilon = E_F)$ vs ε_{diel}. When ε_{diel} is small (<2), F_1^{diel} would be larger, such that the incident electron would see only a single-triangular barrier inside the dielectric (since the barrier at the dielectric–vacuum interface would be below the electron initial energy level), yielding a smaller slope for $F_1 = 6$, 8, and 10 V/nm. The trends of these curves are found to follow closely those of the "area under the curve" in the potential barrier (i.e., WKBJ approximation, see Fig. S5 in the supplementary material).

Figure 2(f) shows the effect of the dielectric electron affinity on photoelectron transmission probability, with $\varepsilon_{diel} = 2$, and $d = 1$ nm. $D(\varepsilon = E_F)$ increases with χ, due to the lowering of the potential barrier. There appears distinct resonance peaks on each curve for a given F_1 due to quantum interference. The peaks shift toward a larger χ as the laser field strength increases, which is indicated by the gray dotted lines in Fig. 2(f). Note that the model recovers photoemission from bare metal surfaces[42,43] when $d = 0$ or when $\chi = 0$ and $\varepsilon_{diel} = 1$ (i.e., vacuum).

Figure 3 shows the effects of dielectric properties on photoemission current density. The photoemission current density J, calculated from Eq. (4), is plotted as a function of dielectric thickness d in Fig. 3(a), for laser field strengths from 2 to 10 V/nm. J decreases with d for $0 < d < 1$ nm. The current density is almost constant for $d > 1$ nm, while there appears some slight resonance peaks, such as the orange dots on the curve for $F_1 = 2$ V/nm. These features are similar to those of dc field emission from dielectric-coated surfaces (cf. Fig. 5 of Ref. 38). The resonances are not as strong as those in Fig. 2(d) for $D(\varepsilon = E_F)$ vs d. This is because photoemission current includes the electron emission from all incident energy levels in the metal, which, in combination, smoothens the curve and reduces the strong emission peaks from a single initial energy level. Note that in our model, electron–phonon scattering and electron–electron scattering effects in dielectrics are not considered. According to the experiment in Ref. 47, a mean free path of a few nanometers has been observed for photoexcited electrons in dielectrics.[47,48] Therefore, for a dielectric thickness smaller than the mean free path, the scattering effect inside the coating may not be important. Figure 3(b) shows J as a function of relative permittivity ε_{diel}. The curves exhibit two distinct slopes in the semilog scale plot, which can be inferred from the transmission probability in Fig. 2(e). Figure 3(c) presents the effect of dielectric electron affinity on photoemission current density. Generally, emission current density increases with electron affinity for a given field strength, due to the lowering of the surface potential barrier. Mild resonant peaks in J are also observed as χ changes.

It is interesting to find that a flat cathode surface with dielectric coating can emit a larger current density than an uncoated

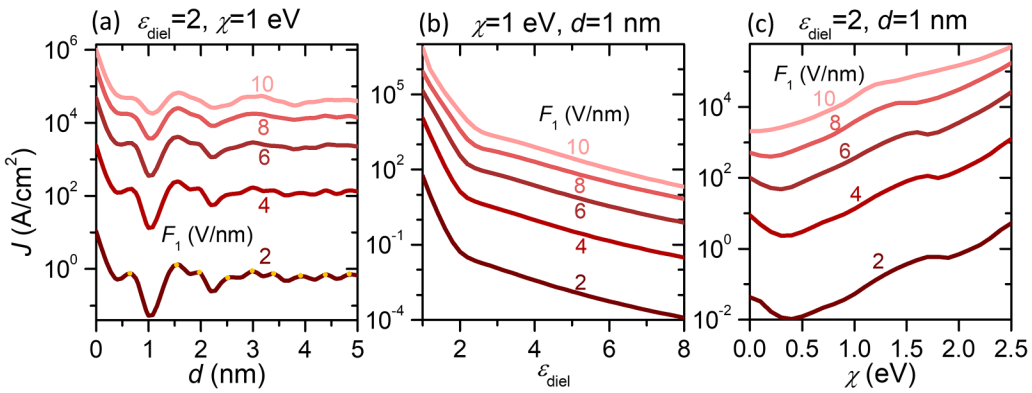

FIG. 3. The photoelectron emission current density J from a dielectric-coated flat metal surface as a function of dielectric properties (a) thickness d; (b) relative permittivity ε_{diel}; and (c) electron affinity χ, for laser field strengths from 2 to 10 V/nm. The dc field $F_0 = 0$, and temperature $T = 300$ K.

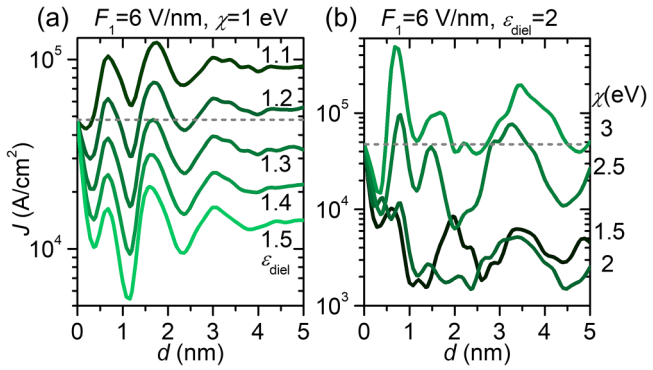

FIG. 4. The photoemission current density J from a dielectric-coated flat metal surface as a function of dielectric thickness d under a different (a) relative permittivity ε_{diel}; (b) electron affinity χ. The dc electric field $F_0 = 0$.

case, when the dielectric has a sufficiently small relative permittivity ε_{diel} or a large electron affinity χ, which would result in a narrowed or lowered potential barrier. Figures 4(a) and 4(b) provide examples of such cases, as shown in the region above the gray dashed lines. A similar electron emission enhancement phenomenon is also demonstrated for field emission from dielectric-coated surfaces.[38] It should be pointed out that the scattering of electrons with phonons, impurities, and even with other electrons inside the dielectric is not considered in the model. Photoelectron emission from ultrathin oxide covered devices shows an exponential attenuation behavior for the relatively thick oxide layer ($2.5 \sim 15.3$ nm), with the dominant mean-free-path of the photoexcited electrons inside $SiO_2 \sim 1.2$ nm.[47] Therefore, for a dielectric thicker than the mean-free-path, electron scattering effects cannot be ignored.

B. Effects of dc field on photoemission

Figure 5 shows the effects of the dc electric field on photoemission from dielectric-coated metal surfaces. The transmission probability through different n channels from initial energy $\varepsilon = E_F$ under a different F_0 is shown in Fig. 5(a). As F_0 increases, the dominant emission channel shifts to a smaller n. The narrowed and lowered (due to the Schottky effect) surface potential barrier by the static field enables more photoemission mechanisms, such as photo-assisted field emission ($1 < n < 4$), multiphoton emission ($n < 0$), and direct tunneling ($n = 0$). The electron transmission probability is greatly enhanced by the dc field.

The electron transmission probability $D(\varepsilon = E_F)$ is plotted as a function of the dc field F_0 in Fig. 5(b) for different laser field strengths. The combined dc field and laser field results in an emission probability significantly larger than that from either field alone. When $F_1 = 0$, the electron transmission probability recovers the dc field emission from dielectric-coated surfaces.[38]

Figure 5(c) shows the emission current density as a function of the dc field under various laser field strengths. The shape of the emission current density is similar to the transmission probability from $\varepsilon = E_F$ in Fig. 5(b). For $F_0 \lesssim 12$ V/nm, the slope of the curves varies with the laser field strength F_1, which indicates that n-photon-assisted field tunneling dominates in this range, where n becomes smaller as F_0 increases. When $F_0 \gtrsim 12$ V/nm, the slopes of the curves for all four cases are almost the same, because the dominant emission becomes dc field tunneling.

IV. COMPARISON WITH THE EFFECTIVE SINGLE-BARRIER MODEL AND MODIFIED DOUBLE-BARRIER FOWLER–NORDHEIM EQUATION

In this section, we compare the results of our exact analytical model with the effective single-barrier quantum model (ESQM)[36] and modified Fowler–Nordheim (FN) equation[40,41] for photoemission from dielectric-coated metal surfaces. The description of the

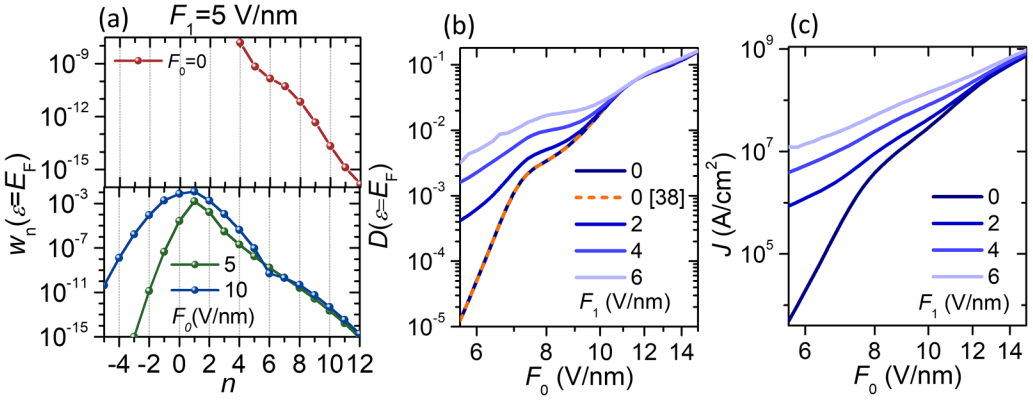

FIG. 5. Effects of dc field on photoemission from dielectric-coated metal surfaces. (a) Photoemission probability through different n-channels from an initial energy level $\varepsilon = E_F$ under various dc fields with a laser field strength $F_1 = 5$ V/nm. (b) Electron transmission probability $D(\varepsilon = E_F)$, and (c) electron emission current density J, as a function of the dc field F_0 under various laser field strengths. The dashed line in (b) is for calculation using Eq. (8) of Ref. 38. The coating has $\varepsilon_{diel} = 2$, $\chi = 1$ eV, and $d = 1$ nm.

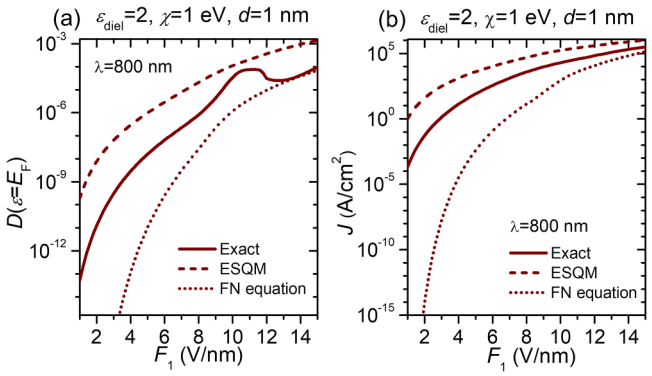

FIG. 6. Comparison of the exact quantum model with the effective single-barrier quantum model (ESQM) and modified Fowler–Nordheim (FN) equation for photoemission from 1D flat dielectric-coated metal surfaces. (a) Transmission probability $D(\varepsilon = E_F)$, and (b) emission current density J, as a function of the laser field strength F_1 in the vacuum. Here, we use $\varepsilon_{diel} = 2$, $\chi = 1$ eV, and $d = 1$ nm. The dc electric field $F_0 = 0$.

ESQM is found in Ref. 36. A short account of the modified FN equation is provided in Appendix B.

Figure 6 shows a comparison of the three models for photoemission from 1D flat cathodes. The electron emission probability $D(\varepsilon = E_F)$ as a function of the laser field strength F_1 is plotted in Fig. 6(a). It can be seen that, for flat surfaces with coating, the ESQM overestimates the photoemission probability, but the modified FN equation underestimates the photoemission probability, as compared with the exact double-triangular barrier model. The ESQM models the double barrier using an effective single-triangular barrier based on the WKBJ approximation,[36] where the effective barrier height is chosen at $W_{eff} = W_0 - \chi$. When $F_1 < 6$ V/nm, the dominant emission process is multi-photon absorption, since the curve scales as $D \propto F_1^{2n}$ from both the ESQM and the exact double-barrier quantum model. Here, $n = 3$ for the ESQM and $n = 4$ for the exact double-barrier model, which is determined by the ratio of the barrier height W_{eff} to the photon energy ($\hbar\omega = 1.55$ eV for a 800 nm laser) in each model, with $W_{eff} = W_0 - \chi = 4.1$ eV for the ESQM and $W_{eff} = W_0 = 5.1$ eV for the exact double-barrier model. The smaller effective potential barrier used in the ESQM also explains the greater transmission probability by the ESQM. The regime of multiphoton absorption is further confirmed by the Keldysh parameter, $\gamma = 4.75$ (Exact) and $\gamma = 5.68$ (ESQM) for $F_1 = 6$ V/nm (see Fig. S9 in the supplementary material). The abrupt slope change at $F_1 \approx 12$ V/nm from the exact model is due to the channel closing effect.[42,49] The underestimation of $D(\varepsilon = E_F)$ from the FN equation is expected, because the FN equation takes account of optical field tunneling only, which is significantly smaller than other n-photon processes in the multiphoton absorption regime. For $13 < F_1 < 15$ V/nm, the curve for the FN equation overlaps with that for the exact model, as the emission enters the optical field tunneling regime.

Figure 6(b) shows emission current density as a function of the laser field strength F_1, showing similar trends as the emission probability in Fig. 6(a). The curves from the three models converge as the laser field increases to 15 V/nm, when the strong optical field tunneling becomes dominant.

A pyramid-shaped plasmonic resonant photoemitter coated with an atomically thick dielectric has been numerically demonstrated to provide an emission current of orders of magnitude larger than a bare photoemitter.[36] The substantially improved photoemission is ascribed to the increased field enhancement by confining the plasmonic field inside the dielectric waveguide along the metal surface. Although the ESQM was used to estimate the photoemission current and has been verified by comparing it with the modified FN equation, it is desirable to calculate photoemission from the exact analytical model. Figure 7 presents emission current density J, calculated from the exact double-barrier quantum model, ESQM, and a modified FN equation for photoemission from the pyramid-shaped gold emitter with SiO_2 coating, as a function of the externally applied laser field strength F_{ext}. Full wave optical simulation shows an approximately linearly decaying laser field inside the dielectric at a resonance wavelength of 608 nm, with the maximum field enhancement factor β at the metal–dielectric interface ($x = 0$ in Fig. 1). To accommodate the double-triangular barrier quantum model and the modified FN equation, the laser field inside the coating is assumed uniform, with the field strength being the one at the metal–dielectric interface, and the laser field in the vacuum is assumed to be that at the dielectric–vacuum interface, i.e., $F_1^{diel} = \beta(x = 0)F_{ext}$, and $F_1 = \beta(x = d)F_{ext}$. Those three models manifest a quantitatively good agreement for $F_{ext} > 0.05$ V/nm, where the emission enters the strong field tunneling regime.[36] This transition is also indicated from the value of the Keldysh parameter approaching unity, $\gamma = 1.89$ (Exact) and $\gamma = 2.46$ (ESQM) for $F_{ext} = 0.05$ V/nm (see Fig. S10 in the supplementary material). For $0.01 < F_{ext} < 0.05$ V/nm, emission current densities calculated from

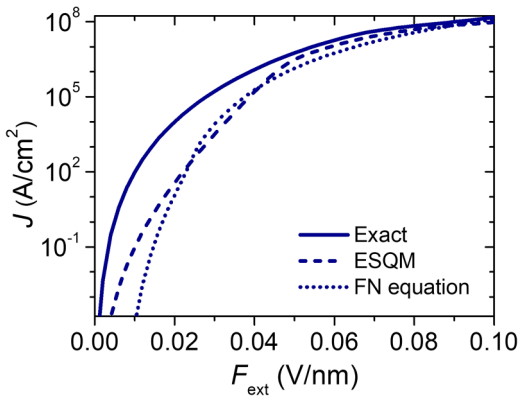

FIG. 7. Photoemission current density J, calculated from the exact double-barrier quantum model (Exact), effective single-barrier quantum model (ESQM), and modified Fowler–Nordheim equation (FN equation), as a function of the externally applied laser field strength F_{ext} for a pyramid-shaped plasmonic resonant photoemitter with SiO_2 coating.[36] Here, the coating thickness $d = 1$ nm, coating electron affinity $\chi = 0.9$ eV, coating relative permittivity $\varepsilon_{diel} = 2.25$, field resonance wavelength is at 608 nm, field enhancement factor at the metal–dielectric interface $\beta(x = 0) = 200$, and field enhancement factor at the dielectric–vacuum interface $\beta(x = d) = 44$.[36] The dc electric field $F_0 = 0$.

both the ESQM and the FN equation are smaller than that from the exact double-barrier model.

One may expect that the assumption of the uniform laser field inside the coating being the maximum field at the metal–dielectric interface would result in an overestimation of the emission current in the small field regime. However, calculation from the exact double-barrier model with F_1^{diel} determined by the slope of the line connecting the peaks of the potential barrier at the two interfaces (see Fig. S6 in the supplementary material) shows that emission current densities from the ESQM and the FN equation are still smaller for $F_{ext} < 0.03$ V/nm, despite the fact that such an approximation of F_1^{diel} would overestimate the potential barrier, thus underestimating photoemission from the exact model. Therefore, applying the ESQM to a dielectric-coated plasmonic resonant Au photoemitter[36] may underestimate the photoemission current for $F_{ext} < 0.03$ V/nm, and the exact double-triangular barrier model may be used to give a more accurate estimation of photoemission from coated photoemitters.

V. CONCLUSIONS

In summary, we have constructed an analytical model for photoemission from metal surfaces coated with an ultrathin dielectric, by exactly solving the one-dimensional (1D) time-dependent Schrödinger equation subject to a double-triangular barrier. The model manifests various electron emission mechanisms, i.e., multiphoton emission, static field tunneling, photon-assisted field emission, optical field tunneling, and thermionic emission, depending on the applied fields (laser field and dc field) and temperature. The effects of dielectric properties on photoemission are investigated. It is found that a flat metal surface coated with a dielectric of smaller relative permittivity and larger electron affinity can photoemit a current density larger than the uncoated metal due to the lowered surface barrier. For dielectric-coated nanoemitters, photoemission can be greatly enhanced due to the nonlinear field enhancements near the coating.

Our model is compared with the effective single-barrier quantum model and modified Fowler–Nordheim equation, for both flat cathodes and three-dimensional (3D) nanoemitters. It is found that both the effective single-barrier model and the modified Fowler–Nordheim equation may underestimate photoemission from the dielectric-coated nanoemitters in the multiphoton absorption regime, and that our exact model may give a more accurate estimation. In the strong-field optical tunneling regime, the three models show quantitatively good agreement. The results further confirm that plasmonic resonant tip photoemitters with thin dielectric coating may be promising for higher yield electron sources.[36]

While a wide range of dc and optical fields are used in this theoretical study of photoemission from 1D flat cathodes, the operation of real-world cathodes poses limitations on the dc field and laser field (intensity, pulse duration, and repetition rate). The breakdown strength for dielectrics shows strong dependence on their relative permittivity and thickness. A theoretical ultimate breakdown strength of 1.5 V/nm for SiO_2 is reported[50] and an optical breakdown laser pulse with a duration of 25 fs and field strength of ~20 V/nm is experimentally observed.[51] Laser pulses can also induce heating and even ablation of the metal, which depend strongly on the laser wavelength, pulse duration, and intensity. A laser pulse of 450 fs duration at 248 nm, with a peak intensity of up to 13.5×10^9 W/cm^2, is experimentally used for photoemission from a polycrystalline copper flat surface, and a nonlinear increase of photocurrent due to the laser heating effects is observed.[52] As the laser duration decreases, the applied intensity can be increased. In Ref. 14, a laser of 14 fs duration, 1.65 μm wavelength, and up to 7.4×10^{13} W/cm^2 intensity (after geometrical field enhancement) is used to study photoemission from single-crystalline gold tips. For realistic nanostructured cathodes or sharp nanoscale emitters, because of the strong field enhancement factor[53,54] and possible further enhancement due to plasmonic resonance,[36] the externally applied laser intensity and dc bias field are expected to be orders of magnitude smaller than those shown in this work for 1D flat surfaces that are considered for simplicity. These important factors should be taken into consideration for the design of practical photocathodes.

In this model, the dielectric is assumed ideal, with only electron affinity and relative permittivity taken into consideration. The metal, the dielectric, and the interfaces between them are all assumed to be perfectly aligned and with no defects or impurities. However, localized traps may exist in the bulk dielectric and at the metal–dielectric interface, especially when the dielectric layer becomes relatively thick,[55] which may result in a trapping of photoexcited electrons from the metal. Trapped charges can have strong effects on photoemission. Experiments show that the reduction of trapped charges by annealing lead to a red shift of the maximum peak of photoemission energy spectrum and the formation of a higher energy plateau.[40] Additionally, the mean free path or the scattering length of electrons within the dielectric is on the order of a few nanometers.[40,41,47,48] As the coating thickness increases, the scatterings (i.e., electron–phonon, electron–electron, electron–impurity) inside the dielectric become important. Future work may consider charge trapping effects as well as scattering effects inside the dielectric in the photoemission model. The effects of space charge[19,21] and pulsed excitation[16] may also be studied in the future.

SUPPLEMENTARY MATERIAL

See the supplementary material for the effects of dielectric properties on photoemission mechanisms, quantum interference inside the dielectric, enclosed area by the potential barrier profile, comparison with an effective single-barrier quantum model and modified double-barrier Fowler–Nordheim equation, and the calculation of the Keldysh parameter.

ACKNOWLEDGMENTS

This work was supported by the Air Force Office of Scientific Research (AFOSR) YIP (Grant No. FA9550-18-1-0061), the Office of Naval Research (ONR) YIP (Grant No. N00014-20-1-2681), and the Air Force Office of Scientific Research (AFOSR) (Grant No. FA9550-20-1-0409).

AUTHOR DECLARATIONS

Conflict of Interest

The authors have no conflicts to disclose.

DATA AVAILABILITY

The data that support the findings of this study are available from the corresponding author upon reasonable request.

APPENDIX A: FORMULATION OF THE DOUBLE-TRIANGULAR BARRIER QUANTUM MODEL

The exact solution to Eq. (2) in the metal ($x < 0$) is

$$\psi_I(x,t) = e^{-\frac{i\varepsilon}{\hbar}t + i\sqrt{\frac{2m\varepsilon}{\hbar^2}}x} + \sum_{n=-\infty}^{\infty} R_{1n} e^{-\frac{i\varepsilon+n\hbar\omega}{\hbar}t - i\sqrt{\frac{2m(\varepsilon+n\hbar\omega)}{\hbar^2}}x}, \quad x<0, \quad \text{(A1)}$$

which represents the superposition of the incident plane wave with an electron incident longitudinal energy ε, and a set of reflected waves with an energy of $\varepsilon + n\hbar\omega$ after photon absorption ($n > 0$) or emission ($n < 0$) processes. R_{1n} is the reflection coefficient.

In the dielectric ($0 \le x < d$), the solution to Eq. (2) is obtained by the following Truscott transformation and separation of variables:[16,42,43,56–59]

$$\psi_{II}(x,t) = \sum_{n=-\infty}^{\infty} T_{2n} \exp\left[i\sqrt{\frac{2m}{\hbar^2}E_{2n}}\left(x + \frac{eF_1^{diel}\cos\omega t}{m\omega^2}\right)\right]\Theta(x,t) + \sum_{n=-\infty}^{\infty} R_{2n}\exp\left[-i\sqrt{\frac{2m}{\hbar^2}E_{2n}}\left(x + \frac{eF_1^{diel}\cos\omega t}{m\omega^2}\right)\right]\Theta(x,t), \quad 0 \le x < d, \quad \text{(A2)}$$

for $F_0 = 0$ or

$$\psi_{II}(x,t) = \sum_{n=-\infty}^{\infty} [T_{2n}[Ai(-\zeta_n) - iBi(-\zeta_n)] + R_{2n}[Ai(-\zeta_n) + iBi(-\zeta_n)]]\Gamma(x,t), \quad 0 \le x < d \quad \text{(A3)}$$

for $F_0 \neq 0$, where T_{2n} and R_{2n} are the transmission coefficient and reflection coefficient of electron waves through the nth channel in the dielectric, respectively; $E_{2n} = \varepsilon + n\hbar\omega - U_{p2} - V_{20}$ is the drift kinetic energy in the dielectric, with the ponderomotive energy $U_{p2} = \frac{e^2(F_1^{diel})^2}{4m\omega^2}$ and $V_{20} = E_F + W - \chi$; $\Theta(x,t) = \exp\left[-i\frac{\varepsilon+n\hbar\omega}{\hbar}t + i\frac{eF_1^{diel}\sin\omega t}{\hbar\omega}x + i\frac{e^2(F_1^{diel})^2\sin 2\omega t}{8\hbar m\omega^3}\right]$; $\Gamma(x,t) = \exp\left[-i\frac{e^2F_0^{diel}F_1^{diel}\sin\omega t}{\hbar m\omega^3}\right]\Theta(x,t)$; $\zeta_n = \left(x + \frac{eF_1^{diel}\cos\omega t}{m\omega^2} + \frac{E_{2n}}{eF_0^{diel}}\right)\left(\frac{2meF_0^{diel}}{\hbar^2}\right)^{1/3}$. ψ_{II} represents the superposition of the forward traveling waves and the reflected waves in the dielectric.

In the vacuum ($x \ge d$), the exact solution to Eq. (2) is

$$\psi_{III}(x,t) = \sum_{n=-\infty}^{\infty} T_{3n}\exp\left[i\sqrt{\frac{2m}{\hbar^2}E_{3n}}\left(x + \frac{eF_1\cos\omega t}{m\omega^2}\right)\right]\Xi(x,t), \quad x \ge d \quad \text{(A4)}$$

for $F_0 = 0$ or

$$\psi_{III}(x,t) = \sum_{n=-\infty}^{\infty} T_{3n}[Ai(-\eta_n) - iBi(-\eta_n)]\exp\left[-i\frac{e^2F_0F_1\sin\omega t}{\hbar m\omega^3}\right] \times \Xi(x,t), \quad x \ge d \quad \text{(A5)}$$

for $F_0 \neq 0$, where T_{3n} is the transmission coefficient in the vacuum; $E_{3n} = \varepsilon + n\hbar\omega - U_{p3} - V_{30}$ is the drift kinetic energy in the vacuum, with the ponderomotive energy $U_{p3} = \frac{e^2F_1^2}{4m\omega^2}$ and $V_{30} = W + E_F + ed(F_0 - F_0^{diel})$ for $F_0 \neq 0$ or $V_{30} = W + E_F$ for $F_0 = 0$; $\Xi(x,t) = \exp\left[-i\frac{ed(F_1 - F_1^{diel})\sin\omega t}{\hbar\omega} - i\frac{\varepsilon+n\hbar\omega}{\hbar}t + i\frac{eF_1\sin\omega t}{\hbar\omega}x + i\frac{e^2F_1^2\sin 2\omega t}{8\hbar m\omega^3}\right]$; $\eta_n = \left(x + \frac{eF_1\cos\omega t}{m\omega^2} + \frac{E_{3n}}{eF_0}\right)\left(\frac{2meF_0}{\hbar^2}\right)^{1/3}$. ψ_{III} denotes the outgoing waves traveling to the vacuum.

Continuity of the wave function and its derivative at both the metal–dielectric interface ($x = 0$) and the dielectric–vacuum interface ($x = d$) and Fourier transform yields the solutions for R_{1n}, T_{2n}, R_{2n}, and T_{3n},

$$\delta(l) + R_{1l} = \sum_{n=-\infty}^{\infty} T_{2n}P_{1n(n-l)} + \sum_{n=-\infty}^{\infty} R_{2n}Q_{1n(n-l)}, \quad \text{(A6)}$$

$$k_0\delta(l) - k_lR_{1l} = \sum_{n=-\infty}^{\infty} T_{2n}P_{2n(n-l)} + \sum_{n=-\infty}^{\infty} R_{2n}Q_{2n(n-l)}, \quad \text{(A7)}$$

$$\sum_{n=-\infty}^{\infty} T_{2n}P_{3n(n-l)} + \sum_{n=-\infty}^{\infty} R_{2n}Q_{3n(n-l)} = \sum_{n=-\infty}^{\infty} T_{3n}Z_{3n(n-l)}, \quad \text{(A8)}$$

$$\sum_{n=-\infty}^{\infty} T_{2n}P_{4n(n-l)} + \sum_{n=-\infty}^{\infty} R_{2n}Q_{4n(n-l)} = \sum_{n=-\infty}^{\infty} T_{3n}Z_{4n(n-l)}, \quad \text{(A9)}$$

where δ is the Dirac delta function; $P_{1nl} = \frac{1}{2\pi}\int_0^{2\pi} P_{1n}(\omega t)e^{-il\omega t}d(\omega t)$, $Q_{1nl} = \frac{1}{2\pi}\int_0^{2\pi} Q_{1n}(\omega t)e^{-il\omega t}d(\omega t)$, $P_{2nl} = \frac{1}{2\pi}\int_0^{2\pi} P_{2n}(\omega t)e^{-il\omega t}d(\omega t)$, $Q_{2nl} = \frac{1}{2\pi}\int_0^{2\pi} Q_{2n}(\omega t)e^{-il\omega t}d(\omega t)$, $P_{3nl} = \frac{1}{2\pi}\int_0^{2\pi} P_{3n}(\omega t)e^{-il\omega t}d(\omega t)$, $Q_{3nl} = \frac{1}{2\pi}\int_0^{2\pi} Q_{3n}(\omega t)e^{-il\omega t}d(\omega t)$, $Z_{3nl} = \frac{1}{2\pi}\int_0^{2\pi} Z_{3n}(\omega t)e^{-il\omega t}d(\omega t)$, $P_{4nl} = \frac{1}{2\pi}\int_0^{2\pi} P_{4n}(\omega t)e^{-il\omega t}d(\omega t)$, $Q_{4nl} = \frac{1}{2\pi}\int_0^{2\pi} Q_{4n}(\omega t)e^{-il\omega t}d(\omega t)$, and $Z_{4nl} = \frac{1}{2\pi}\int_0^{2\pi} Z_{4n}(\omega t)e^{-il\omega t}d(\omega t)$ are the Fourier transform coefficients. For $F_0 = 0$, we have

$$P_{1n}(\omega t) = \exp\left[i\sqrt{\frac{2m}{\hbar^2}E_{2n}}\left(\frac{eF_1^{diel}\cos\omega t}{m\omega^2}\right)\right]\rho(\omega t), \quad \text{(A10)}$$

$$Q_{1n}(\omega t) = \exp\left[-i\sqrt{\frac{2m}{\hbar^2}E_{2n}}\left(\frac{eF_1^{diel}\cos\omega t}{m\omega^2}\right)\right]\rho(\omega t), \quad \text{(A11)}$$

$$P_{2n}(\omega t) = P_{1n}(\omega t)\left[\sqrt{\frac{2m}{\hbar^2}E_{2n}} + \frac{eF_1^{diel}\sin\omega t}{\hbar\omega}\right], \quad \text{(A12)}$$

$$Q_{2n}(\omega t) = Q_{1n}(\omega t)\left[-\sqrt{\frac{2m}{\hbar^2}E_{2n}} + \frac{eF_1^{diel}\sin\omega t}{\hbar\omega}\right], \quad \text{(A13)}$$

$$P_{3n}(\omega t) = \exp\left[i\sqrt{\frac{2m}{\hbar^2}E_{2n}}\left(d + \frac{eF_1^{diel}\cos\omega t}{m\omega^2}\right)\right]\rho(\omega t), \quad \text{(A14)}$$

$$Q_{3n}(\omega t) = \exp\left[-i\sqrt{\frac{2m}{\hbar^2}E_{2n}}\left(d + \frac{eF_1^{diel}\cos\omega t}{m\omega^2}\right)\right]\rho(\omega t), \quad \text{(A15)}$$

$$Z_{3n}(\omega t) = \exp\left[i\sqrt{\frac{2m}{\hbar^2}E_{3n}}\left(d + \frac{eF_1\cos\omega t}{m\omega^2}\right)\right]\varrho(\omega t), \quad \text{(A16)}$$

$$P_{4n}(\omega t) = P_{3n}(\omega t)\left[\sqrt{\frac{2m}{\hbar^2}E_{2n}} + \frac{eF_1^{diel}\sin\omega t}{\hbar\omega}\right], \quad \text{(A17)}$$

$$Q_{4n}(\omega t) = Q_{3n}(\omega t)\left[-\sqrt{\frac{2m}{\hbar^2}E_{2n}} + \frac{eF_1^{diel}\sin\omega t}{\hbar\omega}\right], \quad \text{(A18)}$$

$$Z_{4n}(\omega t) = Z_{3n}(\omega t)\left[\sqrt{\frac{2m}{\hbar^2}E_{3n}} + \frac{eF_1\sin\omega t}{\hbar\omega}\right] \quad \text{(A19)}$$

with $\rho(\omega t) = \exp\left[i\frac{e^2(F_1^{diel})^2\sin 2\omega t}{8\hbar m\omega^3}\right]$ and $\varrho(\omega t) = \exp\left[i\frac{e^2F_1^2\sin 2\omega t}{8\hbar m\omega^3}\right]$.

For $F_0 \neq 0$, we have

$$P_{1n}(\omega t) = s(\zeta_n(x=0))\Upsilon(\omega t), \quad \text{(A20)}$$

$$Q_{1n}(\omega t) = r(\zeta_n(x=0))\Upsilon(\omega t), \quad \text{(A21)}$$

$$P_{2n}(\omega t) = \left[\frac{eF_1^{diel}\sin\omega t}{\hbar\omega}s(\zeta_n(x=0)) + \kappa_2 t(\zeta_n(x=0))\right]\Upsilon(\omega t), \quad \text{(A22)}$$

$$Q_{2n}(\omega t) = \left[\frac{eF_1^{diel}\sin\omega t}{\hbar\omega}r(\zeta_n(x=0)) + \kappa_2 u(\zeta_n(x=0))\right]\Upsilon(\omega t), \quad \text{(A23)}$$

$$P_{3n}(\omega t) = s(\zeta_n(x=d))\Upsilon(\omega t), \quad \text{(A24)}$$

$$Q_{3n}(\omega t) = r(\zeta_n(x=d))\Upsilon(\omega t), \quad \text{(A25)}$$

$$Z_{3n}(\omega t) = v(\eta_n(x=d))\Lambda(\omega t), \quad \text{(A26)}$$

$$P_{4n}(\omega t) = \left[\frac{eF_1^{diel}\sin\omega t}{\hbar\omega}s(\zeta_n(x=d)) + \kappa_2 t(\zeta_n(x=d))\right]\Upsilon(\omega t), \quad \text{(A27)}$$

$$Q_{4n}(\omega t) = \left[\frac{eF_1^{diel}\sin\omega t}{\hbar\omega}r(\zeta_n(x=d)) + \kappa_2 u(\zeta_n(x=d))\right]\Upsilon(\omega t), \quad \text{(A28)}$$

$$Z_{4n} = \left[\frac{eF_1\sin\omega t}{\hbar\omega}v(\eta_n(x=d)) + \kappa_3 w(\eta_n(x=d))\right]\Lambda(\omega t), \quad \text{(A29)}$$

with $\Upsilon(\omega t) = \exp\left[-i\frac{e^2F_0^{diel}F_1^{diel}\sin\omega t}{\hbar m\omega^3} + i\frac{e^2(F_1^{diel})^2\sin 2\omega t}{8\hbar m\omega^3}\right]$, $s(\zeta_n) = Ai(-\zeta_n) - iBi(-\zeta_n)$, $r(\zeta_n) = Ai(-\zeta_n) + iBi(-\zeta_n)$, $t(\zeta_n) = iAi'(-\zeta_n) + Bi'(-\zeta_n)$, $u(\zeta_n) = iAi'(-\zeta_n) - Bi'(-\zeta_n)$, $\kappa_2 = \left(\frac{2meF_0^{diel}}{\hbar^2}\right)^{1/3}$, $\Lambda(\omega t) = \exp\left[-i\frac{e^2F_0F_1\sin\omega t}{\hbar m\omega^3} + i\frac{e^2F_1^2\sin 2\omega t}{8\hbar m\omega^3}\right]$, $v(\eta_n) = Ai(-\eta_n) - iBi(-\eta_n)$, $w(\eta_n) = iAi'(-\eta_n) + Bi'(-\eta_n)$, and $\kappa_3 = \left(\frac{2meF_0}{\hbar^2}\right)^{1/3}$.

APPENDIX B: MODIFIED FOWLER–NORDHEIM EQUATION FOR THE DOUBLE-TRIANGULAR BARRIER

Following the procedure in Ref. 41, a modified Fowler–Nordheim equation is formulated. For the scenario of an ultrathin dielectric on a metal surface, a double step barrier is formed. If the zero of energy is taken at the Fermi level, the lowermost barrier profile bent by the laser field reads

$$V(x,t) = \begin{cases} 0, & x < 0, \\ W_{eff} - eF_1^{diel}(t), & 0 \le x < d, \\ W + ed\left[F_1(t) - F_1^{diel}(t)\right] - eF_1(t)x, & x \ge d, \end{cases} \quad \text{(B1)}$$

where W is the nominal work function of the metal; χ and d are the electron affinity and the thickness of the dielectric, respectively; $W_{eff} = W - \chi$ is the effective work function at the metal–dielectric interface; F_1 and F_1^{diel} are the laser field strengths in the vacuum and in the dielectric, respectively; and e is the positive elementary charge. Note that the dc field is not considered in this modified Fowler–Nordheim equation.

In the current emission calculation, only the positive half cycle of the the laser field is considered. According to the WKBJ approximation, we have the transmission probability

$$D(\varepsilon, F_1) = \exp[Q(\varepsilon, F_1)], \quad \text{(B2)}$$

where $Q(\varepsilon, F_1) = -2\int_0^{x'}\sqrt{2m[V(x)-\varepsilon]/\hbar^2}dx$, m is the effective electron mass, $\hbar$ is the reduced Planck's constant, and x' is such that $V(x) - \varepsilon = 0$. For simplicity, m is set to equal the electron rest mass in all three regions. It is easy to show that

$$Q(\varepsilon, F_1) = -\frac{4}{3}\frac{\sqrt{2m}}{e\hbar F_1^{diel}}\left[(W_{eff}-\varepsilon)^{\frac{3}{2}} - H(W_{eff} - eF_1^{diel}d - \varepsilon) \times (W_{eff} - eF_1^{diel}d - \varepsilon)^{\frac{3}{2}}\right] - \frac{4}{3}\frac{\sqrt{2m}}{eF_1\hbar} \times H(W - eF_1^{diel}d - \varepsilon)(W - eF_1^{diel}d - \varepsilon)^{\frac{3}{2}}. \quad \text{(B3)}$$

Since most of the emission comes from the immediate neighborhood of the Fermi level, we replace $Q(\varepsilon, F_1)$ with the first two terms of the Taylor expansion for $Q(\varepsilon, F_1)$ at $\varepsilon = E_F = 0$, which reads

$$Q(\varepsilon, F_1) = -\frac{4}{3}\frac{\sqrt{2m}W^{\frac{3}{2}}}{e\hbar F_1^{diel}(t)}C + 2\frac{\sqrt{2mW}}{e\hbar F_1^{diel}(t)}B\varepsilon, \quad \text{(B4)}$$

with

$$B = \sqrt{\frac{W_{eff}}{W}} - H(W_{eff} - eF_1^{diel}(t)d)\sqrt{\frac{W_{eff} - eF_1^{diel}(t)d}{W}} + H(W - eF_1^{diel}(t)d)\frac{1}{\varepsilon_{diel}}\sqrt{\frac{W - eF_1^{diel}(t)d}{W}}$$

and

$$C = \left(\frac{W_{eff}}{W}\right)^{3/2} - H(W_{eff} - eF_1^{diel}(t)d)\left[\frac{W_{eff} - eF_1^{diel}(t)d}{W}\right]^{\frac{3}{2}} + H(W - eF_1^{diel}(t)d)\frac{1}{\varepsilon_{diel}}\left[\frac{W - eF_1^{diel}(t)d}{W}\right]^{3/2},$$

where ε_{diel} is the relative permittivity of the dielectric, and $H(x)$ is the Heaviside step function. $F_1^{diel} = F_1/\varepsilon_{diel}$ is used for a perfectly flat dielectric–vacuum interface. The H functions arise from different tunneling scenarios under different field strengths (cf. Fig. 5 in Ref. 40).

The emission current density can be calculated from

$$J = e\int_{-\infty}^{\infty} N(\varepsilon, T)D(\varepsilon, F_1)d\varepsilon. \tag{B5}$$

At a low temperature, $N(\varepsilon, T) = \frac{mk_BT}{2\pi^2\hbar^3}\ln\left[1 + \exp\left(\frac{E_F - \varepsilon}{k_BT}\right)\right] \approx \frac{m}{2\pi^2\hbar^3}(E_F - \varepsilon)$. We finally yield the modified Fowler–Nordheim equation for the double-triangular barrier:

$$J(t) = H[F_1(t)]\frac{e^3F_1^{diel2}(t)}{16\pi^2\hbar WB^2}\exp\left[-\frac{4\sqrt{2m}}{3e\hbar F_1^{diel}(t)}W^{\frac{3}{2}}C\right]. \tag{B6}$$

The time-averaged photoemission current density is

$$J = \frac{\omega}{2\pi}\int_0^{\frac{2\pi}{\omega}} J(t)dt, \tag{B7}$$

where ω is the angular frequency of the laser.

REFERENCES

[1]R. J. England, R. J. Noble, K. Bane, D. H. Dowell, C.-K. Ng, J. E. Spencer, S. Tantawi, Z. Wu, R. L. Byer, E. Peralta, K. Soong, C.-M. Chang, B. Montazeri, S. J. Wolf, B. Cowan, J. Dawson, W. Gai, P. Hommelhoff, Y.-C. Huang, C. Jing, C. McGuinness, R. B. Palmer, B. Naranjo, J. Rosenzweig, G. Travish, A. Mizrahi, L. Schachter, C. Sears, G. R. Werner, and R. B. Yoder, "Dielectric laser accelerators," Rev. Mod. Phys. **86**, 1337–1389 (2014).

[2]J. McNeur, M. Kozak, D. Ehberger, N. Schönenberger, A. Tafel, A. Li, and P. Hommelhoff, "A miniaturized electron source based on dielectric laser accelerator operation at higher spatial harmonics and a nanotip photoemitter," J. Phys. B: At. Mol. Opt. Phys. **49**, 034006 (2016).

[3]T. Hirano, K. E. Urbanek, A. C. Ceballos, D. S. Black, Y. Miao, R. Joel England, R. L. Byer, and K. J. Leedle, "A compact electron source for the dielectric laser accelerator," Appl. Phys. Lett. **116**, 161106 (2020).

[4]P. G. O'Shea and H. P. Freund, "Free-electron lasers: Status and applications," Science **292**, 1853–1858 (2001).

[5]C. Pellegrini, "X-ray free-electron lasers: From dreams to reality," Phys. Scr. **T169**, 014004 (2016).

[6]K. L. Jensen and E. J. Montgomery, "Photoemission theory and the development of high performance photocathodes," J. Comput. Theor. Nanosci. **6**, 1754–1769 (2009).

[7]A. H. Zewail, "Four-dimensional electron microscopy," Science **328**, 187–193 (2010).

[8]E. Najafi, T. D. Scarborough, J. Tang, and A. Zewail, "Four-dimensional imaging of carrier interface dynamics in p-n junctions," Science **347**, 164–167 (2015).

[9]A. Feist, N. Bach, N. Rubiano da Silva, T. Danz, M. Möller, K. E. Priebe, T. Domröse, J. G. Gatzmann, S. Rost, J. Schauss, S. Strauch, R. Bormann, M. Sivis, S. Schäfer, and C. Ropers, "Ultrafast transmission electron microscopy using a laser-driven field emitter: Femtosecond resolution with a high coherence electron beam," Ultramicroscopy **176**, 63–73 (2017).

[10]S. Sun, X. Sun, D. Bartles, E. Wozniak, J. Williams, P. Zhang, and C.-Y. Ruan, "Direct imaging of plasma waves using ultrafast electron microscopy," Struct. Dyn. **7**, 064301 (2020).

[11]S. Vogelgesang, G. Storeck, J. G. Horstmann, T. Diekmann, M. Sivis, S. Schramm, K. Rossnagel, S. Schäfer, and C. Ropers, "Phase ordering of charge density waves traced by ultrafast low-energy electron diffraction," Nat. Phys. **14**, 184–190 (2018).

[12]C. Lemell, X.-M. Tong, F. Krausz, and J. Burgdörfer, "Electron emission from metal surfaces by ultrashort pulses: Determination of the carrier-envelope phase," Phys. Rev. Lett. **90**, 076403 (2003).

[13]A. Apolonski, P. Dombi, G. G. Paulus, M. Kakehata, R. Holzwarth, T. Udem, C. Lemell, K. Torizuka, J. Burgdörfer, T. W. Hänsch, and F. Krausz, "Observation of light-phase-sensitive photoemission from a metal," Phys. Rev. Lett. **92**, 073902 (2004).

[14]B. Piglosiewicz, S. Schmidt, D. J. Park, J. Vogelsang, P. Groß, C. Manzoni, P. Farinello, G. Cerullo, and C. Lienau, "Carrier-envelope phase effects on the strong-field photoemission of electrons from metallic nanostructures," Nat. Photonics **8**, 37 (2014).

[15]Y. Yang, M. Turchetti, P. Vasireddy, W. P. Putnam, O. Karnbach, A. Nardi, F. X. Kärtner, K. K. Berggren, and P. D. Keathley, "Light phase detection with on-chip petahertz electronic networks," Nat. Commun. **11**, 3407 (2020).

[16]Y. Luo, Y. Zhou, and P. Zhang, "Few-cycle optical-field-induced photoemission from biased surfaces: An exact quantum theory," Phys. Rev. B **103**, 085410 (2021).

[17]E. Forati, T. J. Dill, A. R. Tao, and D. Sievenpiper, "Photoemission-based microelectronic devices," Nat. Commun. **7**, 13399 (2016).

[18]P. Zhang and Y. Y. Lau, "Ultrafast and nanoscale diodes," J. Plasma Phys. **82**, 595820505 (2016).

[19]P. Zhang, Á. Valfells, L. K. Ang, J. W. Luginsland, and Y. Y. Lau, "100 years of the physics of diodes," Appl. Phys. Rev. **4**, 011304 (2017).

[20]P. Zimmermann, A. Hötger, N. Fernandez, A. Nolinder, K. Müller, J. J. Finley, and A. W. Holleitner, "Toward plasmonic tunnel gaps for nanoscale photoemission currents by on-chip laser ablation," Nano Lett. **19**, 1172–1178 (2019).

[21]P. Zhang, Y. S. Ang, A. L. Garner, A. Valfells, J. W. Luginsland, and L. K. Ang, "Space-charge limited current in nanodiodes: Ballistic, collisional and dynamical effects," J. Appl. Phys. **129**, 100902 (2021).

[22]F. Rezaeifar, H. U. Chae, R. Ahsan, and R. Kapadia, "Hot electron emission from waveguide integrated lanthanum hexaboride nanoparticles," Appl. Phys. Lett. **118**, 071108 (2021).

[23]Y. Luo and P. Zhang, "Ultrafast optical-field-induced photoelectron emission in a vacuum nanoscale gap: An exact analytical formulation," Appl. Phys. Lett. **119**, 194101 (2021).

[24]D. A. Plemmons, P. K. Suri, and D. J. Flannigan, "Probing structural and electronic dynamics with ultrafast electron microscopy," Chem. Mater. **27**, 3178–3192 (2015).

[25]D. R. Cremons, D. A. Plemmons, and D. J. Flannigan, "Femtosecond electron imaging of defect-modulated phonon dynamics," Nat. Commun. **7**, 11230 (2016).

[26]J. Sun, A. Adhikari, B. S. Shaheen, H. Yang, and O. F. Mohammed, "Mapping carrier dynamics on material surfaces in space and time using scanning ultrafast electron microscopy," J. Phys. Chem. Lett. **7**, 985–994 (2016).

[27]G. Beane, T. Devkota, B. S. Brown, and G. V. Hartland, "Ultrafast measurements of the dynamics of single nanostructures: A review," Rep. Prog. Phys. **82**, 016401 (2019).
[28]N. A. Moody, K. L. Jensen, D. W. Feldman, E. J. Montgomery, and P. G. O'Shea, "Factors affecting performance of dispenser photocathodes," J. Appl. Phys. **102**, 104901 (2007).
[29]N. A. Moody, K. L. Jensen, A. Shabaev, S. G. Lambrakos, J. Smedley, D. Finkenstadt, J. M. Pietryga, P. M. Anisimov, V. Pavlenko, E. R. Batista, J. W. Lewellen, F. Liu, G. Gupta, A. Mohite, H. Yamaguchi, M. A. Hoffbauer, and I. Robel, "Perspectives on designer photocathodes for x-ray free-electron lasers: Influencing emission properties with heterostructures and nanoengineered electronic states," Phys. Rev. Appl. **10**, 047002 (2018).
[30]K. L. Jensen, *Introduction to the Physics of Electron Emission*, 1st ed. (Wiley, Hoboken, NJ, 2017).
[31]F. Liu, N. A. Moody, K. L. Jensen, V. Pavlenko, C. W. Narvaez Villarrubia, A. D. Mohite, and G. Gupta, "Single layer graphene protective gas barrier for copper photocathodes," Appl. Phys. Lett. **110**, 041607 (2017).
[32]A. Tafel, S. Meier, J. Ristein, and P. Hommelhoff, "Femtosecond laser-induced electron emission from nanodiamond-coated tungsten needle tips," Phys. Rev. Lett. **123**, 146802 (2019).
[33]G. Wang, P. Yang, and E. R. Batista, "Computational screening of two-dimensional coatings for semiconducting photocathodes," Phys. Rev. Mater. **4**, 024001 (2020).
[34]H. Ono, J. Miyamatsu, T. Tamba, K. Sakaue, M. Washio, H. Iijima, and H. Zen, "Study on a long-life photocathode with an CsBr protective layer for an rf electron gun," Jpn. J. Appl. Phys. **58**, 066005 (2019).
[35]A. Galdi, W. J. I. DeBenedetti, J. Balajka, L. Cultrera, I. V. Bazarov, J. M. Maxson, and M. A. Hines, "The effects of oxygen-induced phase segregation on the interfacial electronic structure and quantum efficiency of Cs_3Sb photocathodes," J. Chem. Phys. **153**, 144705 (2020).
[36]X. Xiong, Y. Zhou, Y. Luo, X. Li, M. Bosman, L. K. Ang, P. Zhang, and L. Wu, "Plasmon-enhanced resonant photoemission using atomically thick dielectric coatings," ACS Nano **14**, 8806–8815 (2020).
[37]G. Wang, P. Yang, N. A. Moody, and E. R. Batista, "Overcoming the quantum efficiency-lifetime tradeoff of photocathodes by coating with atomically thin two-dimensional nanomaterials," npj 2D Mater. Appl. **2**, 17 (2018).
[38]Y. Zhou and P. Zhang, "Theory of field emission from dielectric coated surfaces," Phys. Rev. Res. **2**, 043439 (2020).
[39]K. L. Jensen, D. Finkenstadt, A. Shabaev, S. G. Lambrakos, N. A. Moody, J. J. Petillo, H. Yamaguchi, and F. Liu, "A photoemission moments model using density functional and transfer matrix methods applied to coating layers on surfaces: Theory," J. Appl. Phys. **123**, 045301 (2018).
[40]P. D. Keathley, A. Sell, W. P. Putnam, S. Guerrera, L. Velásquez-García, and F. X. Kärtner, "Strong-field photoemission from silicon field emitter arrays," Ann. Phys. **525**, 144–150 (2013).
[41]Q.-A. Huang, "Instability of field emission from silicon covered with a thin oxide due to electron trapping," J. Appl. Phys. **79**, 3703–3707 (1996).
[42]P. Zhang and Y. Y. Lau, "Ultrafast strong-field photoelectron emission from biased metal surfaces: Exact solution to time-dependent Schrödinger equation," Sci. Rep. **6**, 19894 (2016).
[43]Y. Zhou and P. Zhang, "A quantum model for photoemission from metal surfaces and its comparison with the three-step model and Fowler–DuBridge model," J. Appl. Phys. **127**, 164903 (2020).
[44]J. G. Simmons, "Generalized formula for the electric tunnel effect between similar electrodes separated by a thin insulating film," J. Appl. Phys. **34**, 1793–1803 (1963).
[45]P. Zhang, "Scaling for quantum tunneling current in nano- and subnano-scale plasmonic junctions," Sci. Rep. **5**, 9826 (2015).
[46]J. Binney and D. Skinner, *The Physics of Quantum Mechanics* (OUP Oxford, 2013).
[47]V. W. Ballarotto, M. Breban, K. Siegrist, R. J. Phaneuf, and E. D. Williams, "Photoelectron emission microscopy of ultrathin oxide covered devices," J. Vac. Sci. Technol., B **20**, 2514 (2002).
[48]Q.-A. Huang, "Field emission from a silicon surface potential well through a thin oxide," J. Appl. Phys. **78**, 6770–6774 (1995).
[49]S. V. Yalunin, M. Gulde, and C. Ropers, "Strong-field photoemission from surfaces: Theoretical approaches," Phys. Rev. B **84**, 195426 (2011).
[50]J. W. McPherson, J. Kim, A. Shanware, H. Mogul, and J. Rodriguez, "Trends in the ultimate breakdown strength of high dielectric-constant materials," IEEE Trans. Electron Devices **50**, 1771–1778 (2003).
[51]M. Mero, J. Liu, W. Rudolph, D. Ristau, and K. Starke, "Scaling laws of femtosecond laser pulse induced breakdown in oxide films," Phys. Rev. B **71**, 115109 (2005).
[52]N. A. Papadogiannis, S. D. Moustaïzis, and J. P. Girardeau-Montaut, "Electron relaxation phenomena on a copper surface via nonlinear ultrashort single-photon photoelectric emission," J. Phys. D: Appl. Phys. **30**, 2389–2396 (1997).
[53]J. Lin, P. Y. Wong, P. Yang, Y. Y. Lau, W. Tang, and P. Zhang, "Electric field distribution and current emission in a miniaturized geometrical diode," J. Appl. Phys. **121**, 244301 (2017).
[54]P. Zhang, S. B. Fairchild, T. C. Back, and Y. Luo, "Field emission from carbon nanotube fibers in varying anode-cathode gap with the consideration of contact resistance," AIP Adv. **7**, 125203 (2017).
[55]E. H. Nicollian and J. R. Brews, *MOS/Metal Oxide Semiconductor/Physics and Technology* (Wiley-Interscience, New York, 1982), p. 920.
[56]W. S. Truscott, "Wave functions in the presence of a time-dependent field: Exact solutions and their application to tunneling," Phys. Rev. Lett. **70**, 1900–1903 (1993).
[57]Y. Luo and P. Zhang, "Ultrafast strong-field photoelectron emission due to two-color laser fields," Phys. Rev. B **98**, 165442 (2018).
[58]Y. Luo and P. Zhang, "Analysis of two-color laser-induced electron emission from a biased metal surface using an exact quantum mechanical solution," Phys. Rev. Appl. **12**, 044056 (2019).
[59]Y. Luo, J. Luginsland, and P. Zhang, "Interference modulation of photoemission from biased metal cathodes driven by two lasers of the same frequency," AIP Adv. **10**, 075301 (2020).

Supplementary Material for

Theory of Laser-induced Photoemission from a Metal Surface with Nanoscale Dielectric Coating

Yang Zhou and Peng Zhang*

Department of Electrical and Computer Engineering, Michigan State University, East Lansing, Michigan 48824-1226, USA

Email: pz@egr.msu.edu

1. *Effects of dielectric properties on photoemission mechanisms*

The electron transmission probability $D(\varepsilon = E_F)$ is shown as a function of the laser field strength F_1 under different dielectric thickness, relative permittivity, and electron affinity in Figs. S1(a), S1(b), and S1(c), respectively. The applied dc electric field F_0 is 0. The electron transmission probability is well scaled as $D(\varepsilon = E_F) \propto F_1^{2n}$, with $n = 4$, in the small laser field range. The sharp slope change of the curves is observed at $F_1 \approx 11.9$ V/nm (see the vertical blue dashed lines in Fig. S1) due to the channel closing effect [1], which indicates the transition from multiphoton absorption to optical field emission. For the chosen parameter ranges, it is found that the dielectric coating has little effects on the laser field strength at which the transition from multiphoton absorption to optical field emission occurs.

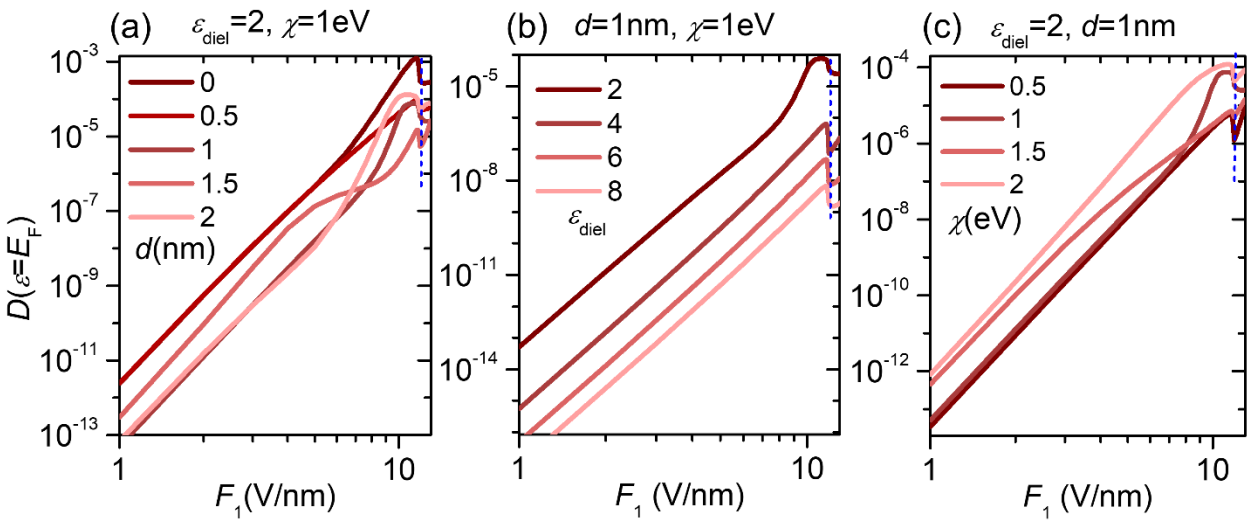

Figure S1. The photoelectron transmission probability $D(\varepsilon = E_F)$ calculated from Eq. (3) in main text, as a function of laser field strength F_1 for different dielectric (a) thickness d; (b) relative permittivity ε_{diel}; and (c) electron affinity χ. The dc electric field $F_0 = 0$.

2. Quantum interference inside the dielectric

The resonance peaks are due to the electron wave interference inside the dielectric [2]. In Fig. S2, the instantaneous electron waves at $t = 0$, including the wave traveling to the dielectric-vacuum interface ψ_{II}^{t}, the wave reflected from the dielectric-vacuum interface ψ_{II}^{r}, as well as the combined wave ψ_{II}, inside the dielectric of various thicknesses, are plotted. A constructive interference is shown in Fig. S2(a) with $d = 2.45$ nm where the resonance peak appears in Fig. 2(d) for $F_1 = 6$ V/nm. The incident wave and reflected wave are almost in phase, especially at distance close to the dielectric-vacuum interface. Figure S2(b) plots the electron waves for $d = 3.8$ nm, which forms a valley point in Fig. 2(d) for $F_1 = 6$ V/nm. The incident wave and reflected wave are ~100 degree out of phase, which results in a small transmission probability.

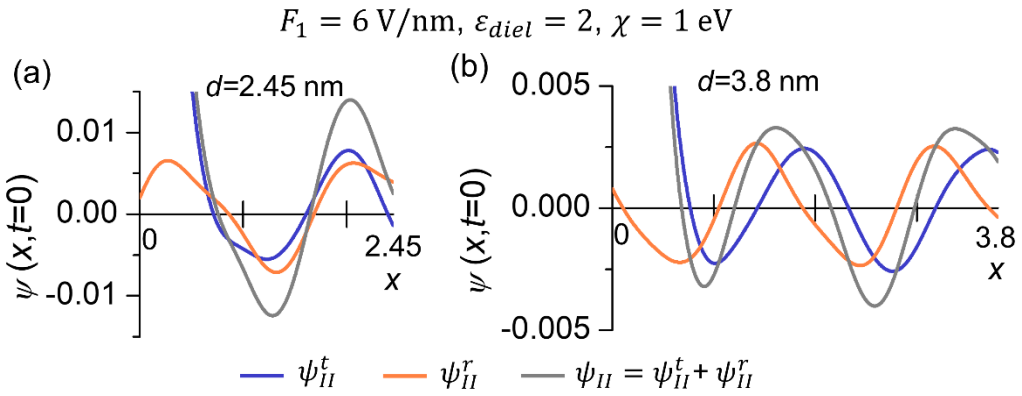

Figure S2. Electron waves inside the dielectric of thicknesses: (a) $d = 2.45$ nm (peak on the curve for $F_1 = 6$ V/nm in Fig. 2(d)); and (b) 3.8 nm (valley on the curve for $F_1 = 6$ V/nm in Fig. 2(d)). The blue curve represents the wave traveling to the dielectric-vacuum interface ψ_{II}^t. The orange curve represents the wave reflected from the dielectric-vacuum interface ψ_{II}^r. The gray curve represents the combination of incident and reflected waves $\psi_{II} = \psi_{II}^t + \psi_{II}^r$. The laser field strength is 6 V/nm. The dielectric has $\chi = 1$ eV and $\varepsilon_{diel} = 2$.

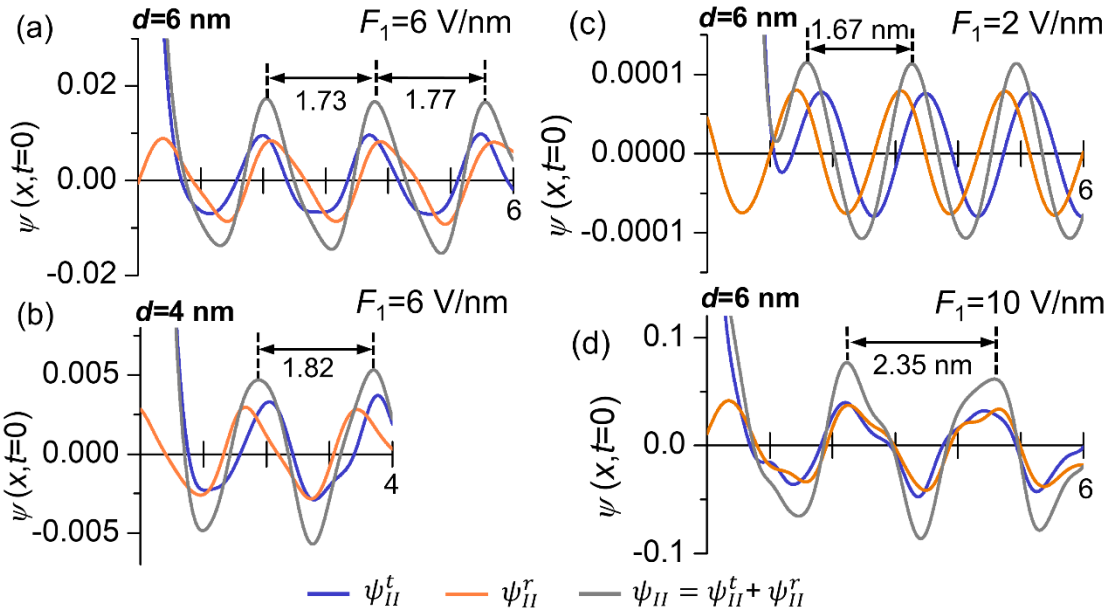

Figure S3. Electron waves for (a) $F_1 = 6$ V/nm and $d = 6$ nm; (b) $F_1 = 6$ V/nm and $d = 4$ nm; (c) $F_1 = 2$ V/nm and $d = 6$ nm; and (d) $F_1 = 10$ V/nm and $d = 6$ nm. The blue curve represents the wave traveling to the dielectric-vacuum interface ψ_{II}^t. The orange curve represents the wave reflected from the dielectric-vacuum interface ψ_{II}^r. The gray curve represents the combination of incident and reflected waves $\psi_{II} = \psi_{II}^t + \psi_{II}^r$. The double arrow line indicates the wavelength between peaks. The dielectric has $\chi = 1$ eV and $\varepsilon_{diel} = 2$.

Note that the wavelength from peak to peak may change slightly for a dielectric of certain thicknesses under a given laser field, as shown in Fig. S3(a). The wavelength varies with dielectric properties, such as thickness shown in Fig. S3(b). The laser field strength also has effects on the wavelength. As F_1 increases, the wavelength increases, as demonstrated in Figs. S3(a), S3(c) and S3(d).

The incident wave and reflected wave inside the dielectric form constructive interference by approximately satisfying the condition,

$$kd = n\pi \text{ or } 2d = n\lambda, \text{with } n = 1, 2, 3 \ldots \quad (S1)$$

where k and λ are the electron wavenumber and the wavelength in the dielectric respectively, and d is the dielectric thickness. Using this condition, with an approximately constant "wavelength" $\lambda = 1.7$ nm obtained from Fig. S3(a), we can predict the dielectric thickness at which interference occurs in the dielectric. The comparison of the predicted resonance thicknesses by Eq. (S1) and the ones from our model which are denoted as blue dots in Fig. S4(a), is provided in Fig. S4(b). Those two results show very good quantitative agreement.

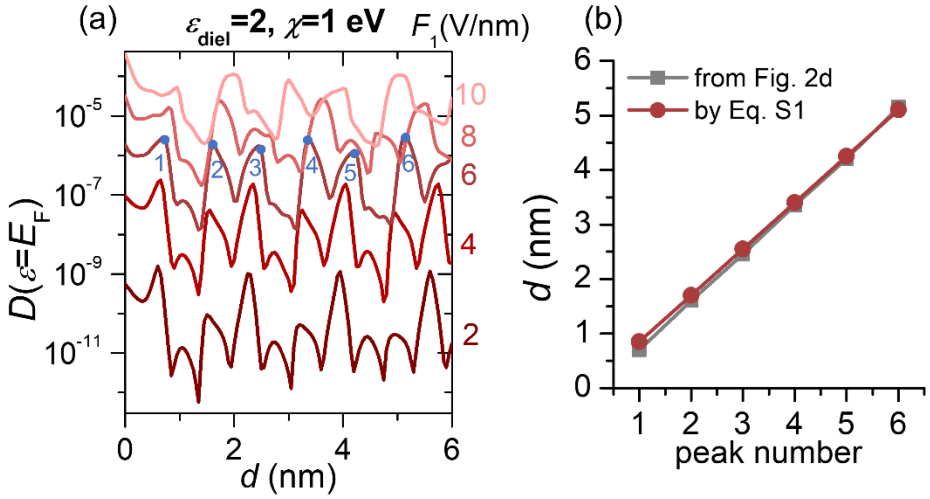

Figure S4. (a) Electron transmission probability as a function of dielectric thickness under various laser field strengths, same as Fig. 2(d) in the main text. Blued dots indicate the resonance peaks for $F_1 = 6$ V/nm. (b) A comparison of the predicted resonance dielectric thickness by Eq. (S1) and resonance dielectric thickness obtained from Fig. 2(d) in main text or Fig. S4(a) here.

3. Enclosed area by the potential barrier profile

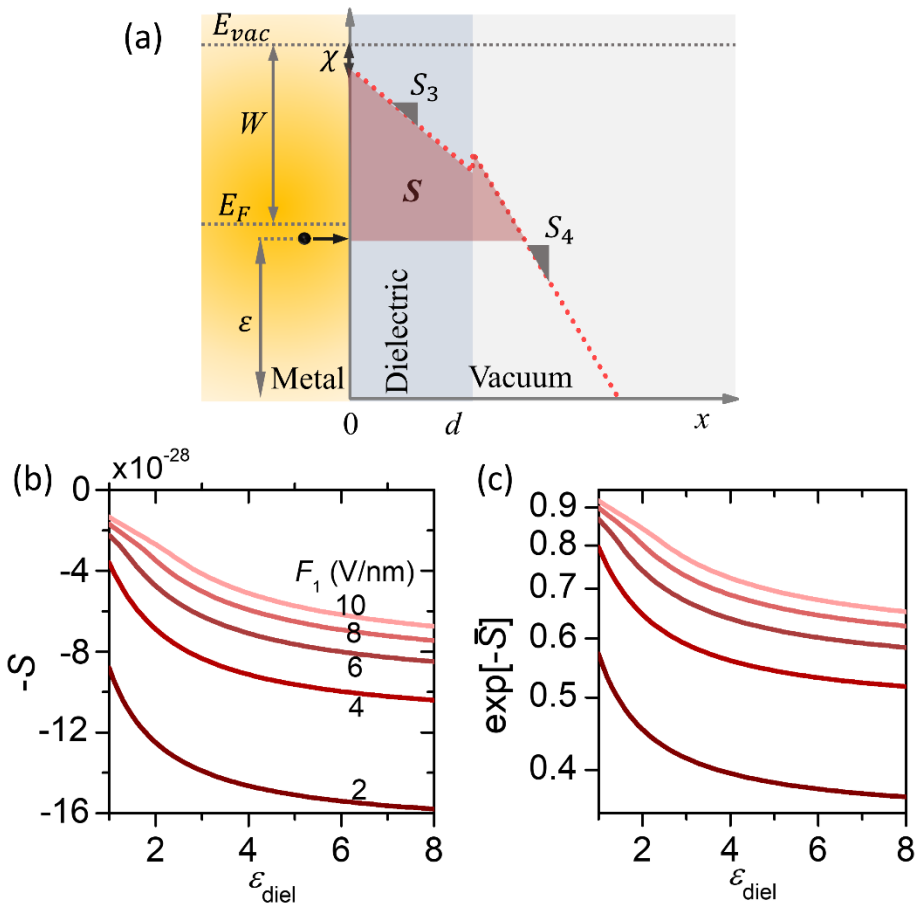

Figure S5. (a) Energy diagram for photoemission from dielectric-coated metal surfaces. The red shaded area denotes the area enclosed by the potential profile (at the time instant of peak laser field) and the electron initial energy ε. (b) Negative S as a function of dielectric relative permittivity under various laser field strengths. (c) Exponential function of negative normalized S as a function of dielectric relative permittivity under various laser field strengths. The area S is normalized to S at $\varepsilon_{diel} = 8$ for $F_1 = 2$ V/nm.

The area enclosed by the potential profile and the electron initial energy provides a good explanation for the slope variation in Fig. 2(e) for electron transmission probability as a function of dielectric relative permittivity. The area reads

$$S = \int_0^{x'} [V(x, t = 0) - \varepsilon] \, dx \qquad (S2)$$

where $V(x, t = 0)$ is the potential barrier provided as Eq. (1) in main text at $t = 0$ with $F_0 = 0$,

ε is the electron initial energy, and x' is such that $V(x, t = 0) - \varepsilon = 0$.

Figures S5(b) and S5(c) plot the negative area S and exponential function of normalized negative S as a function of dielectric relative permittivity under various laser fields. Both plots show a similar trend with Fig. 2(e), especially the slope change for $F_1 = 8$ and 10 V/nm. It is because electrons would face the only triangular barrier inside the dielectric when ε_{diel} is small and F_1 is large enough, since the barrier at the dielectric-vacuum interface would be below ε.

4. *Comparison with effective single-barrier quantum model and modified double-barrier Fowler-Nordheim equation*

Figure S6 presents a comparison of the emission current density J, calculated from the exact double-barrier quantum model, effective single-barrier quantum model (ESQM), and modified Fowler-Nordheim (FN) equation, for the photoemission from the pyramid-shaped gold emitter with SiO_2 coating. To accommodate to the uniform fields in the exact double-barrier model, the laser field inside the coating F_1^{diel} is assumed to be the field determined by the slope of the line connecting the peaks of the potential barrier at the two interfaces (red dotted curve in Fig. S6(a)), and the laser field in the vacuum F_1 is assumed to be the one at dielectric-vacuum interface. In the modified FN equation, F_1^{diel} is the field at metal-dielectric interface, and the laser field in the vacuum is assumed to be the one at dielectric-vacuum interface (blue dotted curve in Fig. S6(a)). Figure S6(b) shows that emission current densities from ESQM and FN equation (blue dashed curve and blue dotted curve) are still lower than the result from the exact double-barrier model (solid red curve) for $F_{ext} \lesssim 0.03$ V/nm, even though such an approximation of field inside the dielectric for the exact model underestimates the photoemission current. Therefore, the emission current density from Au photoemitter with coating may be underestimated by ESQM for $F_{ext} < 0.03$ V/nm, and the exact double-triangular barrier model may be used to give a more accurate estimation.

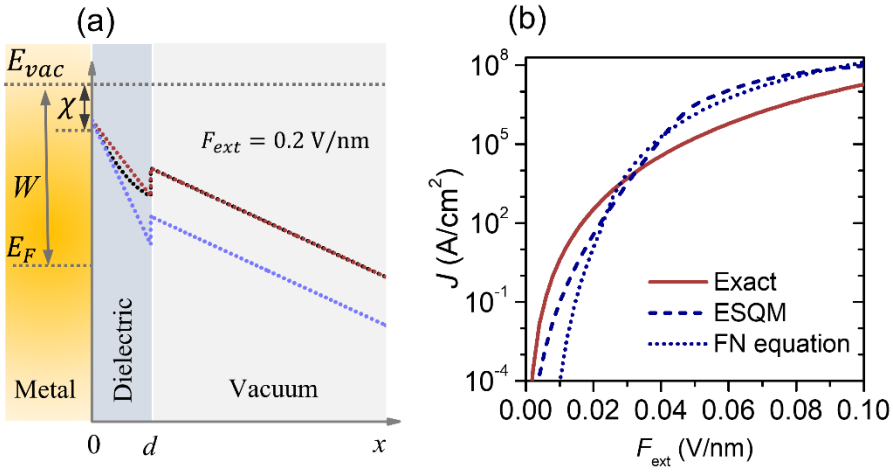

Figure S6. (a) Potential barrier profiles. Black dotted line: original potential profile with laser field profile obtained from full wave optical simulation; red dotted line: approximated potential profile with the uniform laser field in the dielectric determined by the slope of the line; blue dotted line: approximated potential profile with uniform laser field in the dielectric of the field at metal-dielectric interface. The blue dotted line is used in Fig. 7 of the main text. (b) Photoemission current density J, calculated from the exact double-barrier quantum model, effective single-barrier quantum model (ESQM), and modified Fowler-Nordheim equation (FN equation), as a function of externally applied laser field strength F_{ext} for a pyramid-shaped photoemitter with SiO_2 coating. The calculation in the exact model uses the approximate potential profile shown as the red dotted line in (a).

5. *Keldysh parameter* γ

The Keldysh parameter γ is a physical indicator of transition from multiphoton absorption to optical field tunneling in photoemission. γ is estimated as the ratio of two time scales [3-4],

$$\gamma = \frac{4\pi t_t}{T}, \qquad (S3)$$

where $T = 2\pi/\omega$ is the cycle of the optical field, and $t_t = l/v$ is the time of an electron with velocity $v = \sqrt{2W/m}$ tunneling through the potential barrier with a width l, W is the work function of the metal and m is the rest electron mass.

For the case of photoemission from bare metal surfaces, with the instantaneous lower limit

potential profile under a single laser field shown in Fig. S7(a), $\gamma = \omega\sqrt{2mW}/eF_1$. In the effective single-barrier quantum model (ESQM), we calculate the Keldysh parameter as $\gamma = \omega\sqrt{2mW_{eff}}/eF_{eff}$ with $W_{eff} = W - \chi$ and F_{eff} effective laser field determined by the slope of the effective single triangular barrier (refer to [5] for more details). If we follow Keldysh to calculate γ as the ratio of the tunneling time to the optical period, for photoemission from dielectric-coated metal surface, the expression of γ will depend on the laser field strength. When the applied F_1 is relatively small ($W - edF_1^{diel} > 0$), the incident electron has to tunnel through the potential barrier in the vacuum, as shown in Fig. S7(b), and it is found $\gamma = \omega\sqrt{\frac{2m}{W}}\left(W + ed\left(F_1 - F_1^{diel}\right)\right)/eF_1$. When the applied F_1 is relatively large ($W - edF_1^{diel} < 0$), electrons inside the metal can be emitted by tunneling the only potential barrier inside the dielectric, as shown in Fig. S7(c), and we find $\gamma = \omega\sqrt{\frac{2m}{W}}(W - \chi)/eF_1^{diel}$. We will refer using these two expressions to calculate γ as the "exact" method.

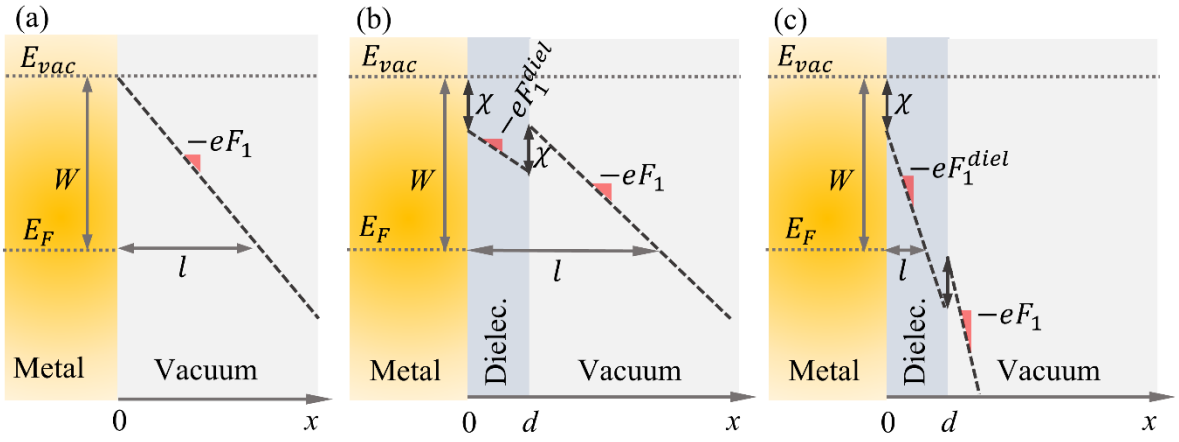

Figure S7. Potential profile for photoemission from (a) bare metal surface; (b) dielectric-coated metal surface under relatively small laser field; (c) dielectric-coated metal surface under relatively large laser field.

The Keldysh parameter γ calculated using the above expressions (i.e. exact method) for the cases in Figs. 2(a), 2(b), and 2(c), as well as cases in Figs. 2(d), 2(e), and 2(f) for $F_1 = 10$ V/nm, is

presented in Fig. S8. It is found that $\gamma > 1$ for all the cases, which confirms the dominant emission process is multiphoton absorption.

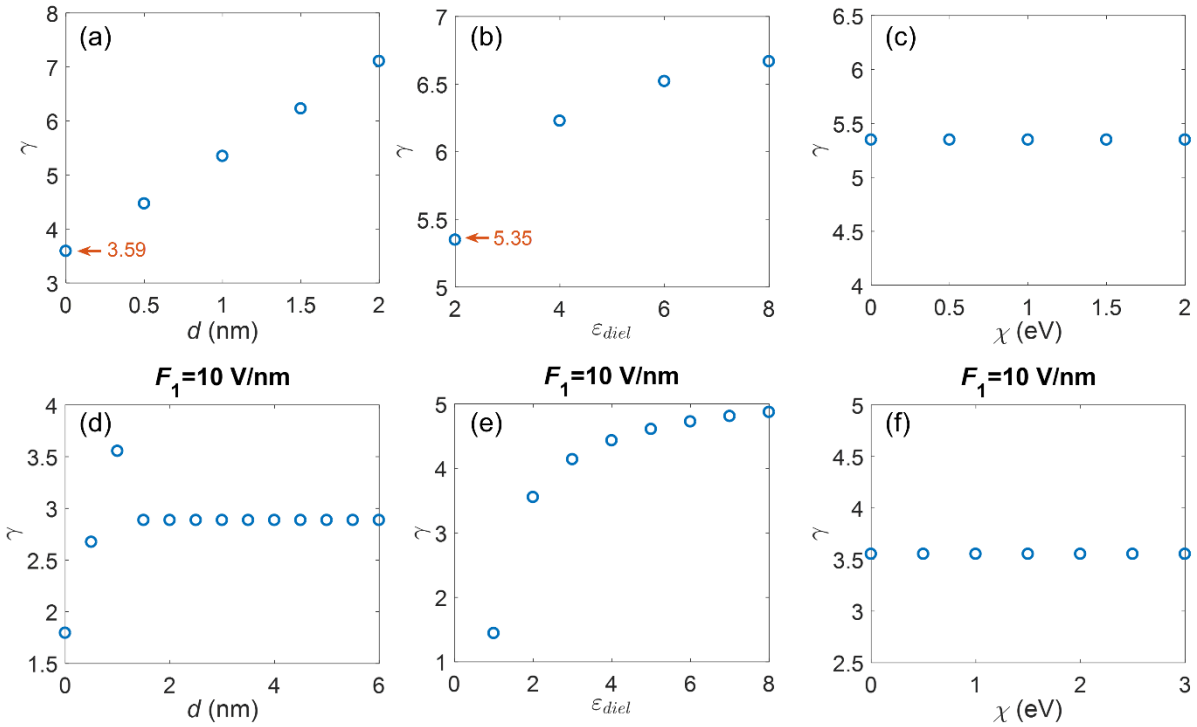

Figure S8. Keldysh parameter γ for the cases in Figs. 2(a), 2(b), and 2(c), as well as the cases in Figs. 2(d), 2(e), and 2(f) for $F_1 = 10$ V/nm.

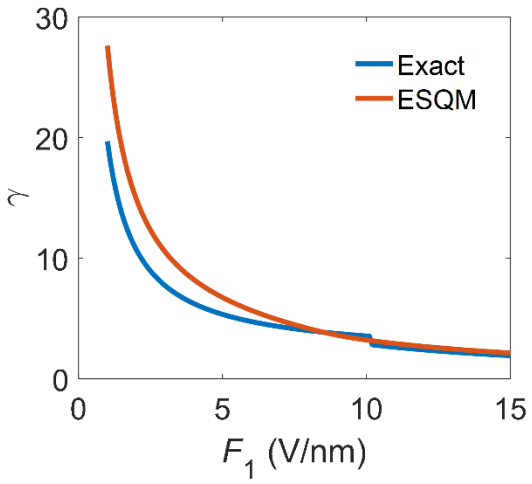

Figure S9. Keldysh parameter γ for the cases in Fig. 6.

Figure S9 shows γ for cases in Fig. 6, with blue curve for the exact quantum model for double triangular barrier and red curve for ESQM. $\gamma = 1.92$ (exact method) and 2.15 (ESQM) at $F_1 = 15$ V/nm.

Figure S10 shows the Keldysh parameter for the cases in Fig. 7. The blue circles represent γ for the exact quantum model for double triangular barrier. The red diamonds represent γ for ESQM. $\gamma \approx 1.14$ (ESQM) and $\gamma = 0.95$ (exact method) at $F_{ext} = 0.1$ V/nm.

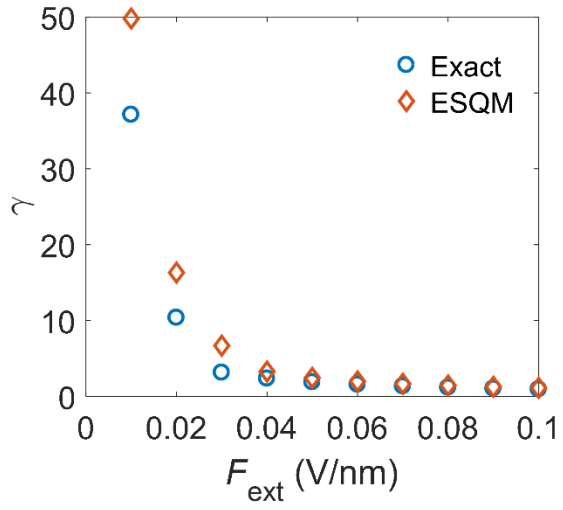

Figure S10. Keldysh parameter γ for the cases in Fig. 7.

References

[1] P. Zhang, and Y. Y. Lau, Sci. Rep. 6, 19894 (2016).

[2] Y. Zhou, and P. Zhang, Phys. Rev. Res. 2, 043439 (2020).

[3] L. V. Keldysh, Zh. Eksp. Teor. Fiz. 47, 1945 (1964) [Sov. Phys. JETP 20, 1307 (1965)].

[4] A. M. Zheltikov, Phys. Rev. A 94, 043412 (2016).

[5] X. Xiong, et al., ACS nano 14(7), 8806-8815 (2020).